Mechanisms of three-dimensional solid-phase epitaxial crystallization of strontium titanate

Tesia D. Janicki,^{†,‡} Rui Liu,[¶] Soohyun Im,[¶] Zhongyi Wan,[†] Serkan Butun,[§] Shaoning Lu,[§] Nasir Basit,[§] Paul M. Voyles,[¶] Paul G. Evans,[¶] and J. R. Schmidt*,[†]

†Department of Chemistry, University of Wisconsin-Madison, Madison, WI 53706

‡Department of Computational Materials, Sandia National Laboratories, Albuquerque, NM

87185

¶Department of Materials Science and Engineering, University of Wisconsin-Madison,

Madison, WI 53706

§Northwestern University Micro/Nano Fabrication Facility, Northwestern University,

Evanston IL, 60208

E-mail: schmidt@chem.wisc.edu

Abstract

Strontium titanate (SrTiO₃, STO) is a complex metal oxide with a cubic perovskite crystal structure. Due to its easily described and understood crystal structure in the cubic phase, STO is an ideal model system for exploring the mechanistic details of solid-phase epitaxy (SPE) in complex oxides. SPE is a crystallization approach that aims to guide crystal growth at low homologous temperatures to achieve targeted microstructures. Beyond planar thin films, SPE can also exploit the addition of a chemically inert, non-crystallizing, amorphous obstacle in the path of crystallization to generate complex three-dimensional structures. The introduction of this mask fundamentally alters the SPE process, inducing a transition from two- to three-dimensional geometries and from

vertical to lateral crystal growth under the influence of the crystal/mask/amorphous boundary. Using a combination of molecular dynamics simulations and experiments, we identify several unique phenomena in the nanoscale growth behaviors in both conventional (unmasked) and masked SPE. Examining conventional SPE of STO, we find that crystallization at the interface is strongly correlated with, and potentially driven by, density fluctuations in the region of the amorphous STO near the crystalline/amorphous interface with a strong facet dependence. In the masked case, we find that the crystalline growth front becomes nonplanar near contact with the mask. We also observe a minimum vertical growth required prior to lateral crystallization. Both phenomena depend on the relative bulk and interfacial free energies of the three-phase (crystal/mask/amorphous) system.

1 Introduction

The crystallization of amorphous solids via solid-phase epitaxy (SPE) is a powerful way to generate complex chemical compositions and structures via controlled crystallization of an initially amorphous thin film. SPE separates the deposition of the amorphous precursor from its subsequent crystallization. Contrasting with homogenous nucleation-and-growth processes, SPE mechanisms rely solely on crystal growth from an epitaxial substrate. The substrate provides a template which directs the structure of the amorphous-to-crystal transformation. Under the influence of the crystalline substrate at low homologous temperature, this method exacts kinetic control over crystallization that is often not available in deposition from the vapor, nor in homogeneous nucleation processes. SPE can be used to synthesize compositions and morphologies that are not easily accessible via competing approaches such chemical vapor deposition or molecular beam epitaxy.

SPE can not only control crystal composition and orientation, but can also be used to generate novel morphologies. ^{2,3} By introducing an inert mask in the path of crystallization, the path of the epitaxy can be changed and guided into intricate geometries. SPE can thus be leveraged to move beyond planar thin films, a case that we term vertical epitaxy. The crystallized structures can have complex three-dimensional geometries, created via lateral overgrowth around or over the mask. Lateral crystallization along the surface of inert barriers has been investigated by Taira et al. ⁴ for Nb-doped anatase TiO₂ to fabricate thin-films over an inert mask layer. More recently, Liu et al. ³ have explored this lateral overgrowth behavior for strontium titanate (SrTiO₃, STO), finding that the stress induced during lateral overgrowth biases the formation of structural defects and yields a systematic rotation of the crystal lattice.

A distinguishing characteristic of SPE in the presence of barriers is the complex crystallization geometry involved when the crystallization transitions from vertical (perpendicular to the substrate) to lateral overgrowth (parallel to the substrate). This "corner-turning" behavior is depicted in Fig. 1. This type of growth proceeds both vertically from the substrate (Fig. 1a) and laterally once the crystallization front has reached the top of the mask (Fig. 1b). Beyond the obvious change in the dimensionality of the crystallization process, the transition from vertical to lateral crystallization introduces a new three-phase interface that does not arise in vertical crystallization. Crystallization along the surface of the mask involves interactions of the crystalline substrate, amorphous precursor, and inert mask. While prior experimental and computational studies have probed the kinetics and mechanism of vertical SPE, much less is known regarding the mechanism of multidimensional crystal growth. The key questions involved are how stress impacts the final crystal structure, ⁵ and details as to how the transition from vertical to lateral overgrowth (i.e., the corner-turning mechanism) proceeds. In this work, we focus on latter questions regarding vertical-to-lateral overgrowth transitions.

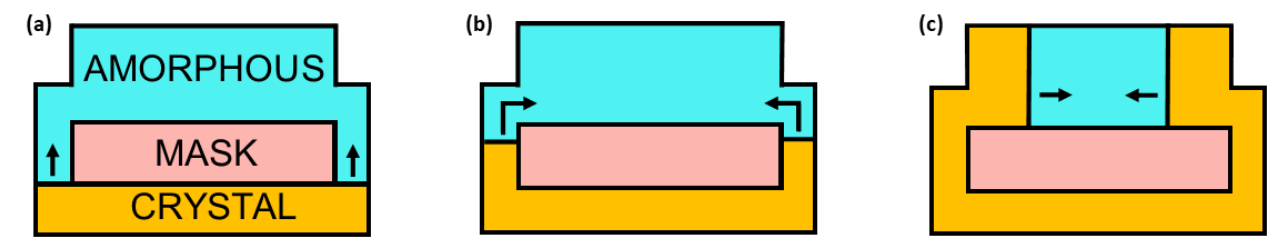


Figure 1: Masked crystal growth with a crystal substrate (orange), inert mask (pink), and deposited amorphous (blue) at successive stages of crystallization.

We use molecular dynamics (MD) simulations to examine the atomistic phenomena arising during the corner-turning process and to identify other phenomena that arise in nanoscale SPE growth. We take STO as a model system because it crystallizes into a single, known, stable structure with $(Pm\bar{3}m)$ symmetry. In addition, each metal ion exhibits, approximately, a single oxidation state $(Sr^{2+} \text{ and } Ti^{4+})$. We have assumed ideal $SrTiO_3$ stoichiometry and have not considered the formation of Ti^{3+} , an excellent approximation for $SrTiO_3$ that has been given sufficient time to equilibrate at high temperatures and at high oxygen partial pressure.^{6,7}

While STO has been extensively studied in epitaxial growth experiments, ^{8,9} computational studies of SPE of complex oxides are challenging because of the relatively long

Prior work has focused on related processes and physical properties such as oxygen vacancy migration, ^{10,11} grain boundary structure and energetics, ¹² and thermal and mechanical properties. ^{13,14} Jesse et al. ¹⁵ modeled the initial stages of heterogeneous homoepitaxy at an elevated temperature. The available duration of the crystallization simulation, approximately 320 ps, was sufficient only to capture the initial interfacial rearrangement at the interface between crystalline and amorphous STO, even at elevated temperatures. ¹⁵ Here we use MD simulations over far longer times, on the order of hundreds of nanoseconds. The longer durations allow the large-scale crystallization of STO to be considered over larger, nanometer-scale distances, to capture three-dimensional phenomena. The work here focuses on comparing the results of simulations with and without an inert mask. With the addition of an inert amorphous gallium nitride (GaN) mask, we introduce additional structures and energies involving the crystal/mask and the amorphous/mask interfaces.

The simulations yield several key insights. First, for the case of vertical epitaxy, the crystallization process is accompanied by density fluctuations in the amorphous phase near the amorphous-crystalline interface. Density fluctuations are, in turn, closely connected to atomic diffusion processes, which suggests that crystallization is influenced or directed by enhanced mass transport at the amorphous-crystal interface. The influence of increased atomic diffusion near the interface has been observed for a similar set of crystallization problems in prior work for Al_2O_3 . In addition, we find that the crystallization velocity depends on the crystal facet orientation, even for low-index interfaces including those in the $\{100\}$, $\{011\}$ and $\{111\}$ families.

In the case of lateral overgrowth, our simulations reveal two key differences from the case of vertical epitaxy: (1) the growth front becomes non-planar near the mask, and (2) the corner turning mechanism requires a minimum vertical growth prior to lateral propagation. These characteristic phenomena of lateral overgrowth can also be explained in terms of the relative interfacial energies. The simulation results are compared with experimental charac-

terization of crystalline/amorphous STO in similar geometries using electron microscopy.

2 Computational Methods

All simulations were carried out in GROMACS 2019.6, ¹⁷ and Ovito ¹⁸ was used for visualization. We employed a Buckingham-style potential (Eq. 1), after Thomas and Marks ¹⁹, for all STO simulations:

$$V_{ij} = A_{ij} exp[-r_{ij}/\rho_{ij}] + \frac{q_i q_j}{4\pi\epsilon_0 r_{ij}},\tag{1}$$

where r_{ij} is distance between atoms i and j and $q_{i/j}$ is the charge on atom i or j. The Born-Mayer parameters A_{ij} and ρ_{ij} were previously fitted to reproduce the cubic perovskite STO crystal structure. Several alternative STO potentials exist in the literature and were also considered, $^{20-22}$ including several models with polarizable shells. Benedek et al. 12 found that, when compared with the results of density functional theory calculations, the added complexity and computational expense of these alternative models did not improve accuracy in predictions of the structure of energies of grain boundaries in STO. We have thus adopted the potential given in Eq. 1 for STO in crystallization studies.

We use a similar Buckingham-style potential for the GaN material used to form the mask in the computational study. The GaN potential uses parameters obtained from Zapol et al. ²³. A dispersion term, $-C_{ij}/r_{ij}^6$, was applied for Ga-Ga and N-N interactions only. Parameters for the STO and GaN potentials are summarized in Table 1. Here, GaN was chosen as a representative non-epitaxial mask, whose principal role is that it does not form an epitaxial relationship with STO. The quantitative details of the GaN-STO interaction were therefore approximated simply using the conventional Lorentz-Berthelot ²⁴ combination rules: geometric mean for A_{ij} and arithmetic mean for ρ_{ij} , ²⁵ with cation-cation interactions (with the exception of Ga-Ga) treated as purely Coulombic.

In both experiment and simulation, the detailed structure of the amorphous precursor material is dependent on the preparation method and thermal history. For our simulations,

Table 1: Buckingham potential parameters for STO and ionic charges (q_{Sr} =1.84e, q_{Ti} =2.36e, and q_O =-1.40e), from Thomas and Marks ¹⁹. Parameters for GaN and ionic charges q_{Ga} =2.0e, q_N =-2.0e, from Zapol et al. ²³

	A_{ij} [eV]	$\rho_{ij} [\text{Å}]$	C_{ij} [eV Å ⁶]
Sr-O	1769.51	0.319894	-
Ti-O	14567.4	0.197584	-
O-O	6249.17	0.231472	-
Sr-Ti	-	-	-
Ga-Ga	6068.14	0.31846	250.
N-N	4115.42	0.31949	280.
Ga-N	872.42	0.31318	0.0

we applied a melt-quench approach and invoked system boundary rescaling to experimental densities in order to best connect with the corresponding experiments. Briefly, STO structures were generated by melting a 1080-atom box at 5000 K and lowering the temperature to 3000 K over 60 ps of simulation using a 1 fs timestep. The system was then equilibrated at 3000 K and the density was rescaled to experiment, 4.2 g cm⁻³, 9 followed by quenching by 2 K ps⁻¹ until the target temperature was reached. The generation of the amorphous structure was concluded by briefly equilibrating at the target temperature.

The melting point for this model, approximately 2300 K (vide infra), is in excellent agreement with the measured experimental value (2313 K²⁶). There are few experimental benchmarks for the amorphous structure of STO. The density provides the most useful point of comparison but unfortunately varies with preparation. We have thus not attempted to tune the potential to match structural studies of amorphous STO. We have, however, verified that the simulated amorphous STO retains no residual long-range order from the initial structure by examining the pair distribution function (PDF). The PDF exhibits features at a scale of 0.3 nm but does not include correlations at the distance scales of crystalline STO.

The crystallization simulations began by briefly equilibrating a 1080-atom cell consisting of $6 \times 6 \times 6$ unit cells of STO, as defined by Meyer et al.²⁷, representing the substrate at the target temperature. The amorphous structure was then appended to the substrate cell using a 0.2 nm initial separation. An additional 3.0 nm vacuum layer was appended to

the top of the amorphous layer. A Cartesian coordinate system was defined so that the z direction corresponded to the direction of vertical crystal growth. Density changes during subsequent crystallization simulations, conducted at constant volume, resulted in an change in the vacuum layer at the top of the simulation cell but did not induce an artificial stress on the system. Atoms within the bottom two unit cells of the substrate in the z-direction were fixed with a harmonic potential to mimic an infinite crystal substrate. x and y of the simulation cells were treated with periodic boundaries. The temperature of SPE simulations was fixed with a Nose-Hoover thermostat with 2 ps coupling time. (110) and (111) surfaces were prepared in a similar way after cleaving along these planes. Note that while some of these facets would yield polar surfaces at a vacuum interface, the rapid equilibration of cations/anions between the crystalline and amorphous surfaces at the interface largely eliminates these concerns in the present case (see Fig. S1 in the Supporting Information).

Simulations with (001)-oriented simulation cells were conducted to find the activation energy of the SPE crystallization from the (001) orientation. These simulations also yielded the melting temperature for STO in this model, forming the basis for the comparison described above. The crystallization simulations had a duration of 300 ns and used a 2 fs timestep. The broadest possible temperature range compatible with this simulation time interval was employed, ranging from 1700 K, for which the crystallization velocity was at the lower limit of the simulation, to 2300 K, above the melting temperature, at steps of 100 K. Frames from these trajectories were saved every 2 ps (1000 steps). Comparisons of the growth velocities of (001), (110), and (111) orientations were performed at 2000 K.

The crystallization velocity was determined by measuring the position of the crystalline-amorphous interface in simulation frames at time intervals of 200 ps. Due to orientational dependence in the crystal structure, a rotationally invariant order parameter is required for structure classification, rather than a simpler collective variable (e.g. RDF peak). As in prior work, ²⁸ we find that the Steinhardt order parameter, ²⁹ (Eq. 2) is a suitable choice

to distinguish between amorphous and crystalline phases,

$$q_l(i) = \left[\frac{4\pi}{(2l+1)} \sum_{l=1}^{l} \left(\sum_{i=1}^{N_i} \frac{Y_{l,m}(r_{ij})}{N_i}\right)^2\right]^{1/2}$$
 (2)

where $Y_{l,m}$ are spherical harmonics and N_i is the number atoms neighboring atom i. The Steinhardt order parameter was computed for the oxygen substructure using l=6; this l value and oxygen substructure were chosen carefully to ensure clear numeric separation between amorphous and crystalline order parameter values. The order parameter q_6 is used extensively, implicitly, throughout the remainder of this work to identify the interface position, which is defined as the inflection point of a binned q_6 profile along the direction of growth. The position of these inflections, corresponding to the amorphous-crystalline interface, were then plotted as a function of time, with linear regression used to measure the growth velocity.

Amorphous GaN was chosen as an inert mask for use in the simulations due to its high melting point, ensuring that the mask would not flow at the annealing temperatures. We also selected GaN for the simulation due to the availability of analogous interatomic potentials. The corresponding experimental measurements used an alternative amorphous material with similar properties (silicon nitride, Si_3N_4) to form the mask. We expect our conclusions to be qualitatively independent of the details of the composition and structure of the mask material because both GaN and Si_3N_4 are amorphous and the resulting STO crystallization thus does not have an epitaxial relationship with the mask. The simulated amorphous GaN was produced in a similar method as amorphous STO, using a 1920-atom GaN box. A simulation volume consisting of a thin film of patterned regions of GaN was produced by superimposing the GaN box into a 12,960-atom (initially $24 \times 6 \times 18$ unit cell) amorphous STO system, with overlapping STO atoms deleted. The stoichiometry was checked prior to simulation to ensure that Sr, Ti, and O atoms remained in a 1:1:3 ratio. The amorphous GaN-STO structure was then appended to a $24 \times 6 \times 6$ unit-cell crystal substrate, as for

homoepitaxial films. Harmonic spring constraints were used to hold the GaN mask in place to ensure rigid edges and corners of this region, even at elevated annealing temperatures.

3 Experimental Methods

Experimental studies of the lateral crystallization of STO were conducted using a patterned STO (001) substrate. The substrate was patterned with 10 μ m × 10 μ m, and 12-nm-thick amorphous Si₃N₄ masks using optical lithography, creating an array across the substrate. A 30-nm-thick amorphous STO layer was deposited on the patterned surface using sputter deposition. Y-ray photoelectron spectroscopy (XPS) was employed to confirm the Ti⁴⁺ oxidation state in the amorphous STO film; details of these measurements are included in the SI.

The amorphous STO layer was crystallized at 823 K at atmospheric pressure in air. The crystallized STO was characterized using transmission electron microscopy (TEM). TEM sample preparation involved coating the specimen with a carbon protection layer, followed by the creation of a thin section employing Focused Ion Beam (FIB) lithography and lift-out techniques. A Zeiss Auriga FIB system was used for conventional lift-out preparation of the TEM specimen, with ion beam energies set at 30 keV for the milling process and 2 keV for subsequent thinning. Final cleaning of TEM specimen was performed using a Fischione Nanomill at energies of 900 eV and 500 eV. High-angle annular dark field (HAADF) imaging data was acquired with the transmission electron microscope operated at 200 kV, with a collection angle ranging from 90 to 250 mrad.

4 Results & Discussion

4.1 Vertical Crystallization

Simulations of the vertical SPE case provide insights and reference points for the interpretation of subsequent lateral overgrowth simulations. The velocity of crystallization as a function of temperature is shown in Fig. 2. The uncertainty in the velocity was determined using the variation among at least three simulations with independent initial velocity distributions at each temperature. The crystallization velocity has an Arrhenius temperature dependence, as shown by the fit in Fig. 2, with an activation energy of interfacial growth equal to 1.1 eV \pm 0.1 eV. The simulations were conducted at far higher temperatures (1900-2200 K) than the experimental studies for which activation energies have been previously reported (typically 600-900 K). Although the experimental crystallization temperatures are much lower, we find that the calculated activation energy of 1.1 ± 0.1 eV from our simulations falls within the range of experimental values, 8,9,30-32 approximately 0.8 to 2.1 eV measured in experiments. The experimental activation further depends on issues not addressed in these simulations, including the gas environment in which crystallization is conducted, with higher activation energies observed in vacuum. ³¹ Previous studies of the crystallization of γ -Al₂O₃ have indicated that the thermally activated processes determining the rate of crystallization occur at the crystalline/amorphous interface. 16 We hypothesize that a similar interfacial effect may determine the crystallization rate in STO. Given the agreement of the activation energy determined from simulation with the range previously observed in experiments, we now turn to using the simulations results to probe the atomistic details of the crystallization process.

The orientation-dependence of the crystallization velocity plays a vital role in 3D crystallization geometries. The crystallization velocity for the low-index interfaces between crystalline and amorphous STO is shown in Fig. 3. An analysis of the simulation results starting with different substrate orientations reveals that different orientations exhibit varying growth

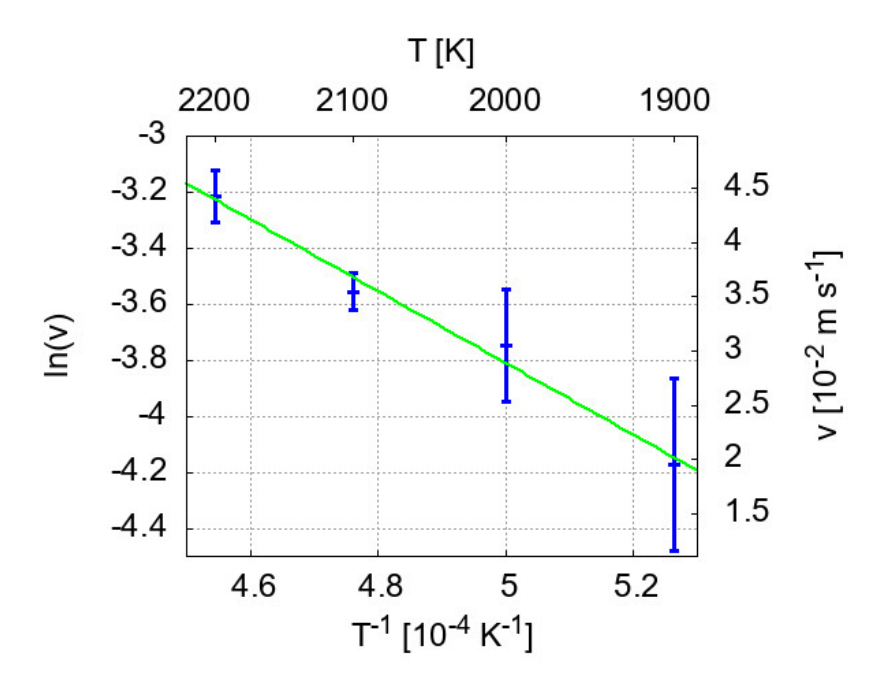


Figure 2: Temperature dependence of the crystallization velocity determined using MD simulations at temperatures from 1900 to 2200 K for (001)-oriented STO. The line shows the Arrhenius fitting of the growth velocity from, with an activation energy of 1.1 eV.

velocities. Velocities were computed at 2000 K and averaged over at least 20 replica simulations in each growth direction. Growth velocities were (2.7 ± 0.2) , (2.1 ± 0.2) , and (1.6 ± 0.2) 10^{-2} nm/ns, for the (001), (110) and (111) orientations respectively.

Qualitatively, experiments suggest that the surface energies of the facets increase as (001), (110), and (111).^{33,34} We find agreement in that our slowest growth velocities occur for the highest surface energies. This is consistent with the correlation of growth velocities and surface free energies for distinct crystal facets, which has been previously reported in both single-element and complex oxide nanocrystals.^{35,36}

In order to obtain insight into the mechanistic details of the epitaxial crystallization, we tracked the evolution of local density throughout the process of crystallization. The local density at the interface was calculated at 2000 K for the (001) orientation. The density variation was studied by computing the number density of oxygen atoms in a volume with a depth of 0.7 nm extending along z into the amorphous STO from the amorphous-crystalline interface. This local oxygen density was calculated during the entire course of a crystalliza-

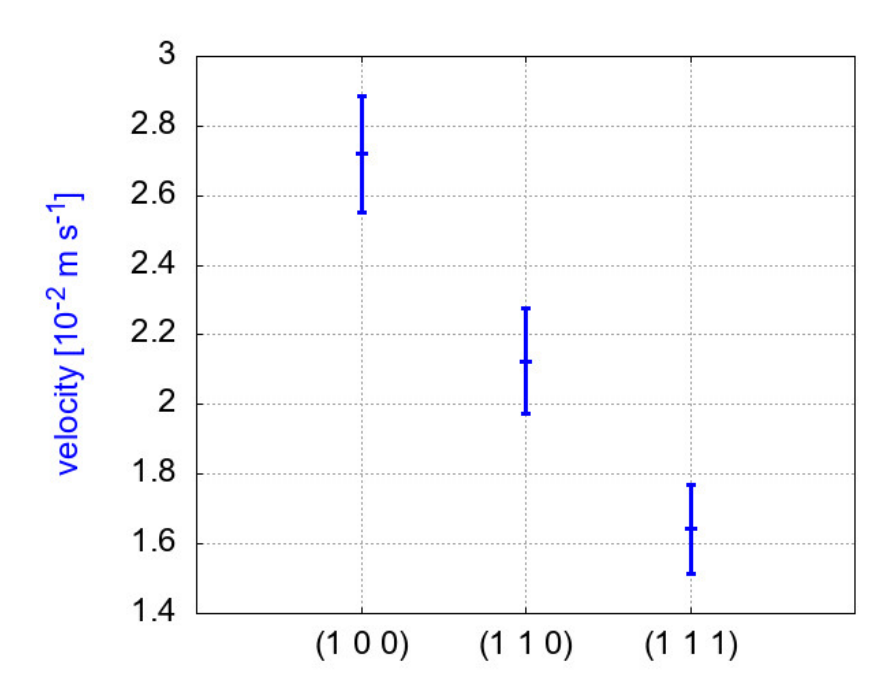


Figure 3: Crystallization velocity at (001), (110), and (111) amorphous/crystalline STO interfaces at 2000 K.

tion simulation. The number density of oxygen atoms was converted to a total mass density by assuming that the amorphous material is uniformly stoichiometric.

The density is both highly spatially non-uniform near the interface and strongly time dependent. This effect is illustrated using the density for a part of the crystallization simulation in Fig. 4. The two frames show configurations before and after a "burst" of crystal growth front propagation separated by an interval of 200 ps. Higher-density regions within the amorphous STO (appearing in red in Fig. 4) approach the crystalline density during transient fluctuations. These fluctuations occur in the bulk of the amorphous region and also near the interface. In the bulk of the amorphous layer, the fluctuations occur throughout the entire duration of the simulation but do not persist to impact the net density of the amorphous layer, nor do these fluctuations become ordered to constitute a homogeneous nucleation event. Near the interface, density fluctuations immediately above the interface, however, appear to be correlated with a brief increase in the growth velocity. While simulations here occur at elevated temperatures relative to experiment, there is still little bulk

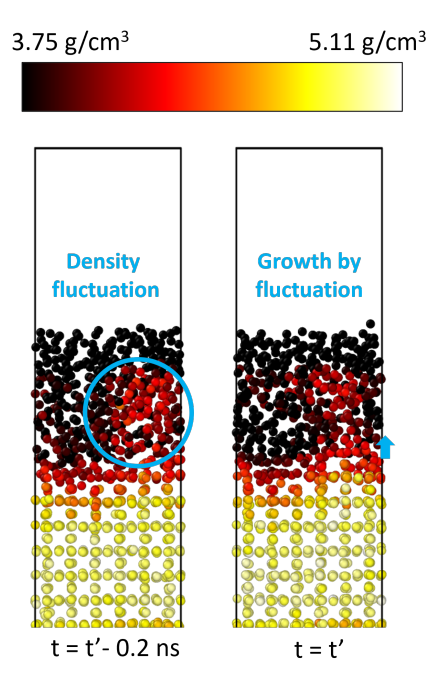


Figure 4: Snapshots of spatial fluctuations of the computed total density immediately prior to growth "burst." For clarity, only oxygen atoms are shown.

diffusion, defining the regime of SPE versus liquid-phase epitaxy, so these sustained density fluctuations near the interface are salient pre-growth features. Fig. 4 shows an example of a fluctuation preceding a burst of crystallization that spatially coincides with the density fluctuation. The rate of local growth fluctuations obtained across a 2D grid of the lateral interface confirmed, as expected, that these fluctuations are spatially uniform across the interface, on average. Fig. 4 also appears to show a persistent region with a (higher) density, intermediate between the amorphous and crystalline densities, at the amorphous-crystalline interface. However, this apparently local variation of density arises from local averaging between amorphous and crystalline volumes in this region.

The correlation between density fluctuations and crystallization was quantified via a cross-correlation between number density, ρ , and growth velocity, v:

$$C_{v\rho}(t) = \frac{\langle \delta v(t) \delta \rho(0) \rangle}{\sqrt{\sigma_v \sigma_\rho}} \tag{3}$$

where

$$\delta A = A - \langle A \rangle. \tag{4}$$

The growth velocity was computed from the rate of change of interface position, as previously described. The oxygen number density was calculated at each time step in the region within 0.7 nm of the computed interface, encompassing the entire lateral simulation cell dimensions.

At the melting temperature the crystalline and amorphous phases are in equilibrium and we must have $C_{v\rho}(0) = 0$. This follows because in equilibrium, as at the melting temperature, the density and atomic velocity are uncorrelated due to the separability of position and velocity within the partition function. At temperatures below the melting temperature, coexisting interfacial system spontaneously crystallizes and is thus outside of equilibrium and the correlation may become nonzero. An analysis of the simulation results shows that at 2000 K, $C_{v\rho} = 0.17$. This nonzero, positive value suggests that density fluctuations near the interface are in fact correlated with enhanced crystal growth. Prior work of Al₂O₃ concludes that enhanced mass transport of ions to the interface over relatively short distances is a driving factor in vertical SPE growth; this mass transport results in an elevated crystallization velocity at low temperature, far higher than would be expected from an extrapolation from the bulk-transport limited rate observed at temperatures close to the melting point. 16 The simulations here reveal that a similar phenomenon arises during vertical epitaxy of STO, emphasizing the crucial role of interfacial processes in amorphous STO during crystallization. Beyond oxides, interfacial diffusion effects have been noted in a variety of systems, ranging in complexity from silicon ³⁷ to organic glasses. ^{38,39} This phenomenon is, therefore, a relatively general feature of epitaxial crystallization processes, rather than a unique feature of STO or Al₂O₃. Our density analysis suggests that transient densification of the amorphous region near the interface precedes, and perhaps even drives, crystal growth.

4.2 Crystallization in a Nanopatterned Geometry

Having examined the mechanistic details of vertical epitaxy, we take these insights to examine the early stages of lateral overgrowth. A key phenomenon in the latter involves the transition between vertical and lateral growth, the "corner turning" event, as sketched in Fig. 1b. We focus on the evolution of the three-phase crystalline/mask/amorphous interface during the corner turning event to understand the details of this transition.

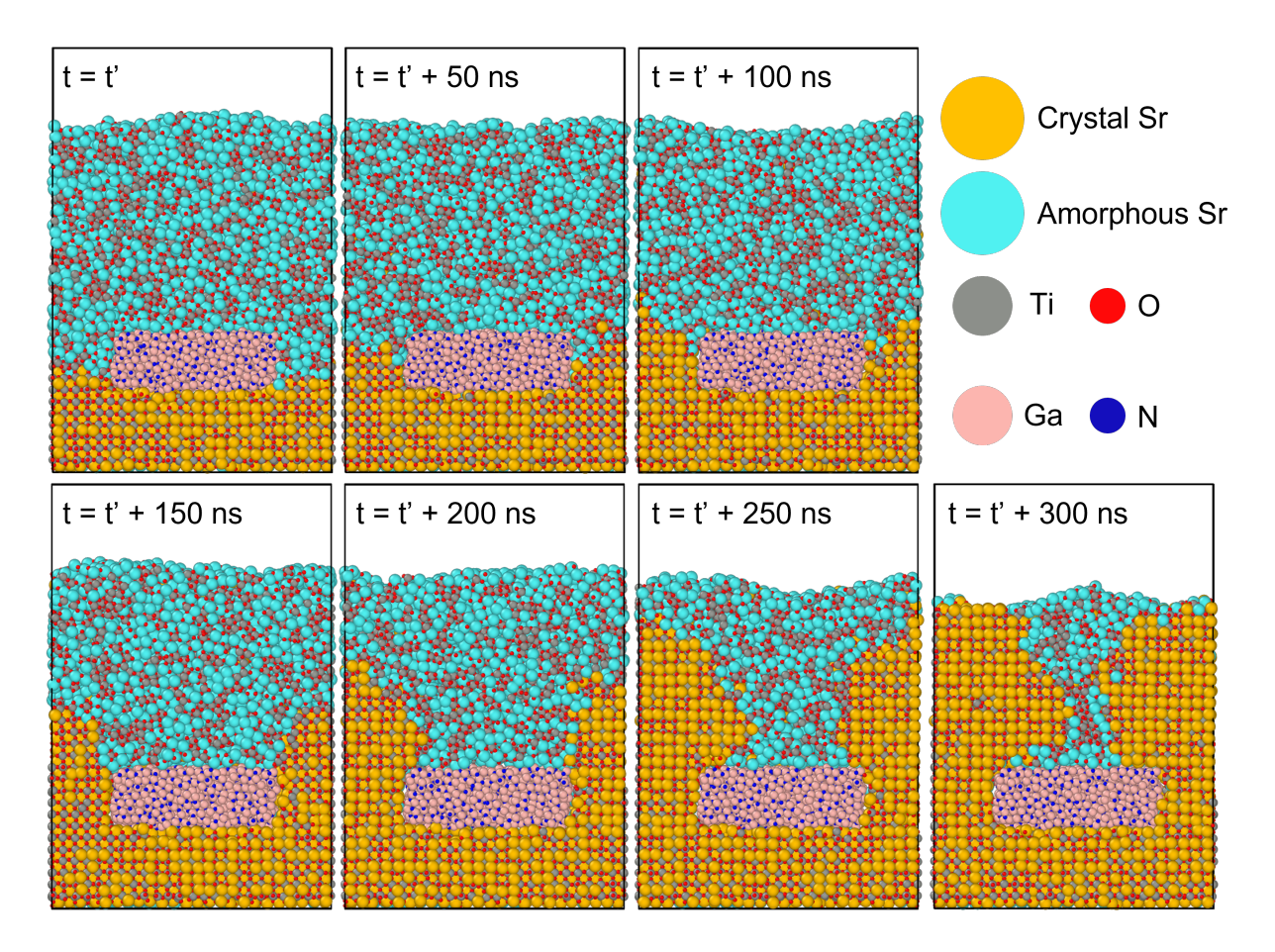


Figure 5: Snapshots of (010) cross-section during the simulated 300 ns duration of the crystallization of amorphous STO grown on (001) STO substrate with GaN mask. Sr atoms are shown in orange in crystalline regions and in blue in amorphous regions to highlight the position of the interface.

The growth of STO in the presence of a masked substrate is shown over a 300 ns trajectory at 2000K in Fig. 5. Initially, crystallization progresses, constrained by the mask, very similarly to the vertical case. At the top of the mask, however, lateral and vertical growth

compete. As expected, we find the rates of lateral and vertical growth to be identical within statistical uncertainty reported for (001) growth reported in Section 4.1, which is intuitive as (001) and (100) orientations are symmetrically identical in STO.

It is apparent from the simulation snapshots in Fig. 5 that the amorphous/crystalline interface is not perpendicular to the direction of growth. This effect is particularly apparent in snapshots at 150, 200, and 250 ns. Instead, the amorphous STO near the GaN mask crystallizes more slowly than in regions further from the mask. The contact angle of the interface with the mask, $\sim 45^{\circ}$, is independent of inter-mask distance (the width of unmasked STO) and roughly corresponds to the (110) orientation. As described above, (110) is the next most stable growth facet and next fastest direction of growth.

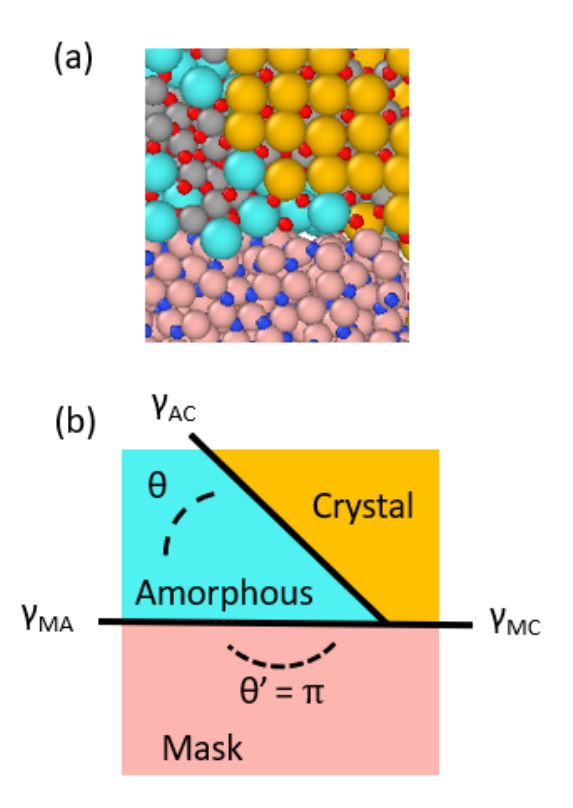


Figure 6: (a) Simulation snapshot depicting contact angle of the amorphous/crystalline, amorphous/mask, and crystalline/mass interface. Atom colors follow Fig. 5. (b) Construction for contact angle calculation.

The orientation of the interface observed in Fig. 5 can be interpreted via an argument based on the expected contact angles arising from the interfacial energies of amorphous STO,

crystalline STO, and the GaN mask. The contact among the three regions is shown in detail in Fig. 6a. We consider these interfacial energies in the context of the boundary at the intersection of three phases as defined by Hirth ⁴⁰. This construction is shown in Fig. 6b, where γ terms are the interfacial energies associated with mask/amorphous, amorphous/crystalline, and mask/crystalline interfaces. Applying these values to the general case discussed by Hirth ⁴⁰ (and taking $\theta' = \pi$, since the mask planar), we obtain Eq. 5, a simple expression for the contact angle, θ , as a function of the three interfacial energies,

$$\theta = \cos^{-1}\left(\frac{\gamma_{mc} - \gamma_{ma}}{\gamma_{ac}}\right) \tag{5}$$

The result is identical to the Young equation, ⁴¹ which predicts the contact angle of solid-gas-liquid systems for surface wettability. Relevant interfacial energies are listed in Table 2, which, applied to Eq. 5, yields $\theta = 46.0(1)^{\circ}$, consistent with the (110) facet. We thereby conclude that the presence of a non-perpendicular contact angle is due to a preference of the mask for contact with the amorphous over the crystal.

Table 2: Computed interfacial energies, 0K

	γ [eV nm ⁻²]
amorphous-crystal (ac)	18.6(6)
mask-amorphous (ma)	12.3(9)
mask-crystal (mc)	25.2(8)

Cross-sectional TEM characterization of the experimentally crystallized layer, Fig. 7, reveals several features that are consistent with the simulation. The region characterized in Fig. 7 includes (i) an area of vertical epitaxy at the left edge of the image, (ii) a region of the transition from vertical to lateral epitaxy, (iii) lateral crystallization of 450 nm, and (iv) the amorphous/crystalline interface. All of these features are consistent with the simulation, including the corner-turning between the regions of vertical and lateral epitaxy. We focus, in particular, on the crystalline/mask/amorphous contact, at which a non-orthogonal contact angle was observed, similar to the simulation results. In the TEM image in Fig. 7, this angle

is approximately 45° to the surface of the mask. Note the experimental angle has an error of \pm 10°, partly due to the limited spatial resolution of the image in Fig. 7. A further difference between the simulation and measurement is in the mask materials: GaN for simulation and Si₃N₄ for experiment. Using GaN in simulation instead of Si₃N₄, may lead to an, as yet unknown, difference in interfacial energy due to composition and structure. Despite these differences, the prediction of an observable contact angle during crystallization appears to be robust.

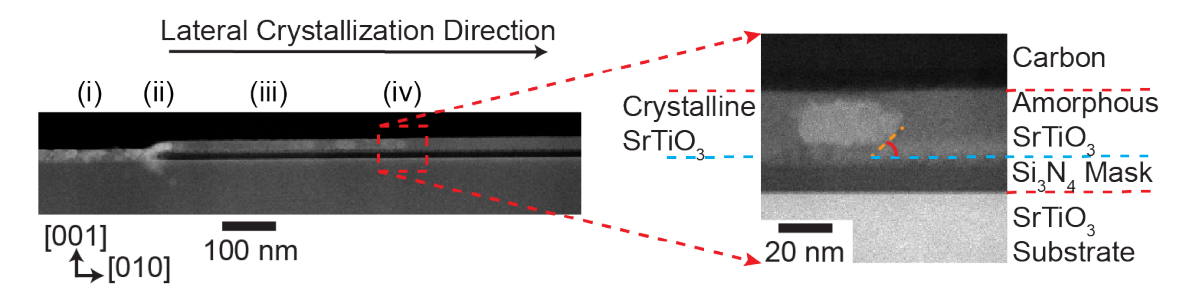


Figure 7: HAADF image showing the lateral crystallization of STO over a $\mathrm{Si}_3\mathrm{N}_4$ mask. Regions of (i) vertical crystallization, (ii) the corner-turning transition from vertical to lateral crystallization, (iii) lateral crystallization, and (iv) the amorphous crystallization are indicated above the image. The right panel is an enlarged view of the area within the red box in the left panel, showing the carbon protection layer (top), interfaces among crystalline and amorphous STO, the $\mathrm{Si}_3\mathrm{N}_4$ mask, and the STO substrate. The delineated angle, highlighted in red, is formed by the intersection of the orange line (crystalline/amorphous STO contact) and the blue line ($\mathrm{Si}_3\mathrm{N}_4$ mask surface), measuring approximately 45°.

A second observation arises from an examination of the atomistic details of the lateral overgrowth. We find that there is a minimum vertical distance above the top of the mask prior to the initiation of lateral growth. This effect is shown in Figs. 8a and 8b. The two frames, Figs. 8a and 8b, show, respectively, the state of the crystallized STO prior to lateral overgrowth and after lateral growth proceeds for a distance of one unit-cell length above the mask. We hypothesize that the minimum vertical crystallization distance prior to lateral growth arises from interfacial energy effects. Specifically, the interfacial energy associated with lateral overgrowth causes vertical growth to be favored initially. Figures 8c and 8d, schematically show the transition from vertical to lateral overgrowth after a vertical growth distance h above the surface of the mask. For simplicity, we consider a final state

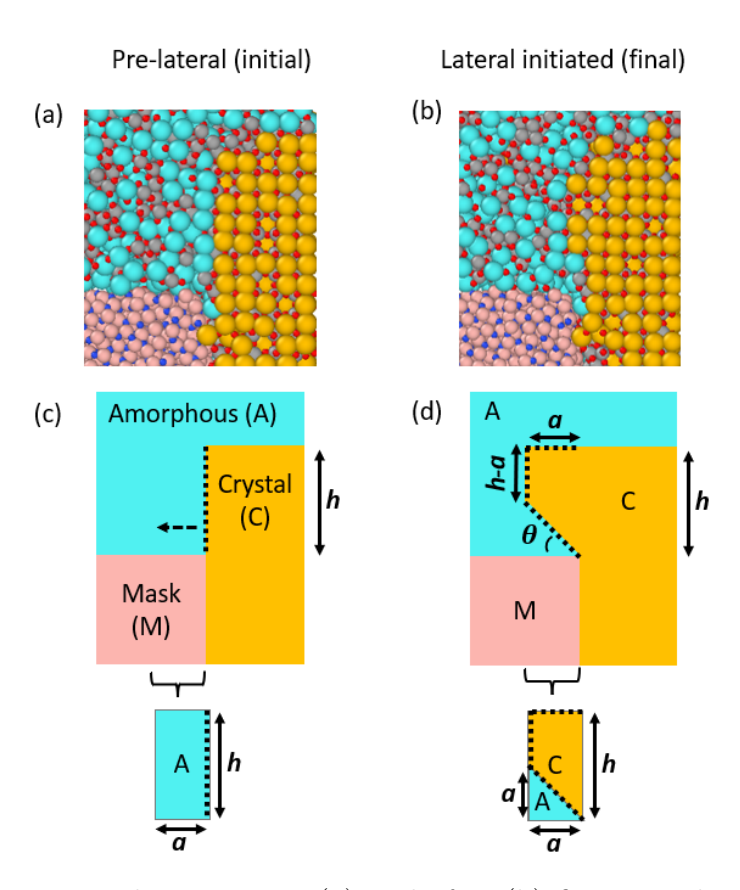


Figure 8: Simulation snapshots prior to (a) and after (b) first monolayer of lateral growth. Atom colors follow Fig. 5. Corresponding schematic sketches (c, initial) and (d, final) illustrate the relevant distances/variables.

when lateral growth has progressed one unit cell length (a=0.3905 nm). Following prior discussion, lateral growth incorporates a contact angle (θ) with the mask. To simplify the geometry, we round this computed angle to 45°. Growth in the lateral direction is favorable only when the minimal distance (h) has crystallized, as defined by the turning point in system free energy (ΔG), arising from a competition between the bulk free energy change upon crystallization ($\Delta \mu = -1.06(1)$ eV per unit cell, approximated at 0K) and the energetic cost associated with interface formation (various γ). Eq. 6 summarizes the free energy difference between the initial and final states in the first step of lateral overgrowth,

$$\Delta G = \gamma_{AC,100} \left(A_{f,100} - A_{i,100} \right) + \gamma_{AC,110} \left(A_{f,110} - A_{i,110} \right) + \frac{\Delta \mu_{A \to C}}{a^3} \left(V_{cryst} \right) \tag{6}$$

where $A_{i/f}$ represents the initial/final surface areas of the specified facets, and V_{cryst} is the

volume of the resulting crystalline phase.

Substituting values defined in Fig. 8, we obtain Eq. 7. The orthogonal depth coordinate (d), which represents the thickness of the system, is included for completeness. At the initial time defined in this calculation, $A_{i,110} = 0$.

$$\Delta G = \gamma_{AC,100}([d \times a + d \times (h - a)] - [d \times h]) + \gamma_{AC,110}([d \times a\sqrt{2}] - [0]) + \frac{\Delta \mu_{A \to C}}{a^3}(d \times h \times a - d \times \frac{a^2}{2})$$
 (7)

This expression reduces to:

$$\frac{\Delta G}{d * a} = \gamma_{AC,110} \sqrt{2} + (h - \frac{a}{2}) \frac{\Delta \mu_{A \to C}}{a^3},\tag{8}$$

which is dependent on only a *single* interface energy between the (110) facet and amorphous.

Solving for the condition $\Delta G = 0$, we find

$$\frac{h}{a} = \frac{1}{2} - \frac{a^2 \gamma_{AC,110} \sqrt{2}}{\Delta \mu_{A \to C}} \tag{9}$$

We use the energy of the crystal-amorphous interface ($\gamma_{AC,110} = 31.6(4)$ eV nm⁻²) and thermodynamic driving force ($\Delta\mu_{A\to C}$), to estimate that the minimum area of contact required for lateral growth is generated once the crystal front has proceeded a length (h) of 7 unit cells (~ 2.6 nm) into the amorphous layer. This estimate does not incorporate the influence of local strain present in the masked system but is sufficient for a first approximation to identify the qualitative origin of observed minimal vertical distance. Our calculated estimate is in good agreement with the 7-8 unit cell distance visually observed in atomistic trajectories (see Fig. 8(a)-(b)). Consequently, we conclude that the origin of the observed minimum vertical distance is entirely a function of relative interfacial energies.

5 Conclusions

We have used classical MD simulations to examine the mechanistic details of both vertical SPE growth of an STO thin film and lateral overgrowth of an inert mask. We find that crystallization during the annealing of the as-deposited amorphous STO follows an Arrhenius temperature dependence with an activation energy of 1.1 eV. The MD results are consistent with prior experimental measurements at lower annealing temperatures. ³² In addition, the crystallization is correlated with (and possibly driven by) density fluctuations in the amorphous in the vicinity of the crystalline-amorphous interface, highlighting the potential importance of mass transfer in this crystallization, as has been seen in related oxide systems. ¹⁶ The agreement between the experimental and simulation results indicates that similar density fluctuations may arise in experiment and suggests that the experimental characterization of interfacial fluctuations (e.g. using electron or x-ray based techniques) could be an impactful direction for experiments.

The simulations incorporating a patterned mask probe lateral overgrowth during SPE. Lateral growth in similar patterned environments can yield three-dimensional crystalline morphologies. We observe two phenomena that are unique to the case of lateral overgrowth:

(1) a non-planar growth front in the vicinity of the mask, and (2) a delay in the initiation of lateral overgrowth at the top of the mask. We conclude that both of these phenomena can be explained in terms of the relative interfacial energies of the three-phase crystalline/mask/amorphous system. In the former case, we find TEM evidence for the existence of non-planarity, consistent with these predictions. In the latter case, the interfacial energies result in a minimum (critical) thickness of the overgrown layer prior to lateral overgrowth. However, given the small (nm) size of this "critical" thickness, experimental confirmation would likely be more challenging. An aspect not addressed in this work is the interface-joining mechanism, when the two growth fronts coalesce over the mask. Rigorous investigation of coalescing interfaces and possible out-of-phase boundaries ⁴² would require larger simulation scales but poses an intriguing future direction for unravelling patterned

6 Associated Content

Supporting Information is available. Fig. S1 depicts visualization of surface charge damping near the (111) interface. Fig. S2 and subsequent discussion provides XPS confirmation of the Ti⁴⁺ oxidation state in the amorphous STO film.

7 Acknowledgements

This research was primarily supported by NSF through the University of Wisconsin Materials Research Science and Engineering Center (DMR-1720415). Support for final revisions and analysis of the TEM data and for facilities and instrumentation was provided by NSF through the University of Wisconsin Materials Research Science and Engineering Center (DMR-2309000). This work made use of the NUFAB facility of Northwestern University's NUANCE Center, which has received support from the SHyNE Resource (NSF ECCS-2025633), the IIN, and Northwestern's MRSEC program (NSF DMR-2308691).

TDJ was affiliated with the University of Wisconsin-Madison Department of Chemistry during the completion of this work. TDJ acknowledges support by the National Science Foundation Graduate Research Fellowship under Grant No. DGE-1747503. Any opinion, findings, and conclusions or recommendations expressed in this material are those of the authors(s) and do not necessarily reflect the views of the National Science Foundation.

TDJ is currently affiliated with Sandia National Laboratories. Sandia National Laboratories is a multi-mission laboratory managed and operated by National Technology & Engineering Solutions of Sandia, LLC (NTESS), a wholly owned subsidiary of Honeywell International Inc., for the U.S. Department of Energy's National Nuclear Security Administration (DOE/NNSA) under contract DE-NA0003525. This written work is authored by an employee of NTESS. The employee, not NTESS, owns the right, title and interest in and to

the written work and is responsible for its contents. Any subjective views or opinions that might be expressed in the written work do not necessarily represent the views of the U.S. Government. The publisher acknowledges that the U.S. Government retains a non-exclusive, paid-up, irrevocable, world-wide license to publish or reproduce the published form of this written work or allow others to do so, for U.S. Government purposes. The DOE will provide public access to results of federally sponsored research in accordance with the DOE Public Access Plan.

References

- (1) Janicki, T. D.; Wan, Z.; Liu, R.; Evans, P. G.; Schmidt, J. R. Guiding epitaxial crystallization of amorphous solids at the nanoscale: interfaces, stress, and precrystalline order. J. Chem. Phys. 2022, 157, 100901.
- (2) Evans, P. G.; Chen, Y.; Tilka, J. A.; Babcock, S. E.; Kuech, T. F. Crystallization of amorphous complex oxides: New geometries and new compositions via solid phase epitaxy. Curr. Opin. Solid State Mater. Sci. 2018, 22, 229–242.
- (3) Liu, R. et al. Optical and electronic functionality arising from controlled defect formation in nanoscale complex oxide lateral epitaxy. Sci. Adv 2024, accepted.
- (4) Taira, K.; Hirose, Y.; Nakao, S.; Yamada, N.; Kogure, T.; Shibata, T.; Sasaki, T.; Hasegawa, T. Lateral Solid-Phase Epitaxy of Oxide Thin Films on Glass Substrate Seeded with Oxide Nanosheets. ACS Nano 2014, 8, 6145–6150.
- (5) Rudawski, N. G.; Jones, K. S.; Morarka, S. Stressed multidirectional solid-phase epitaxial growth of Si. J. Appl. Phys 2009, 105, 81101.
- (6) Chan, N. H.; Sharma, R. K.; Smyth, D. M. Nonstoichiometry in SrTiO₃. J. Electrochem. Soc. 1981, 128, 1762.

- (7) Siebenhofer, M.; Baiutti, F.; de Dios Sirvent, J.; Huber, T. M.; Viernstein, A.; Smetaczek, S.; Herzig, C.; Liedke, M. O.; Butterling, M.; Wagner, A.; Hirschmann, E.; Limbeck, A.; Tarancon, A.; Fleig, J.; Kubicek, M. Exploring point defects and trap states in undoped SrTiO₃ single crystals. *J. Eur. Ceram. Soc.* **2022**, *42*, 1510–1521.
- (8) White, C. W.; Boatner, L. A.; Slkad, P. S.; McHargue, C. J.; Rankin, J.; Farlow, G. C.; Aziz, M. J. Ion-implantation and annealing of crystalline oxides and ceramic materials. Nucl. Instrum. Meth. B 1988, 32, 11–22.
- (9) Chen, Y.; Yusuf, M. H.; Guan, Y.; Jacobson, R. B.; Lagally, M. G.; Babcock, S. E.; Kuech, T. F.; Evans, P. G. Distinct Nucleation and Growth Kinetics of Amorphous SrTiO₃ on (001) SrTiO₃ and SiO₂/Si: A Step toward New Architectures. ACS Appl. Mater. Interfaces 2017, 9, 41034–41042.
- (10) Qu, H.; Luo, B.; Bian, S.; Yue, Z. Thermally stimulated relaxation and behaviors of oxygen vacancies in SrTiO3 single crystals with (100), (110) and (111) orientations.

 Mater. Res. Express 2020, 7, 046305.
- (11) Waldow, S. P.; De Souza, R. A. Computational Study of Oxygen Diffusion along a[100] Dislocations in the Perovskite Oxide SrTiO₃. ACS Appl. Mater. Interfaces 2016, 8, 12246–12256.
- (12) Benedek, N. A.; L-S Chua, A.; Elsässer, C.; Sutton, A. P.; Finnis, M. W. Interatomic potentials for strontium titanate: An assessment of their transferability and comparison with density functional theory. *Phys. Rev. B* **2008**, *78*, 064110.
- (13) Tosawat, S.; Gjindara, W.-U.-D.; Chanchana, T.; Vittaya, A. Molecular Dynamics Simulation of Strontium Titanate. *Chin. Phys. Lett.* **2010**, *27*, 026501.
- (14) Fong Goh, W.; Yoon, T. L.; Khan, A. Molecular dynamics simulation of thermodynamic and thermal transport properties of strontium titanate with improved potential parameters. *Comput. Mater. Sci.* **2012**, *60*, 123–129.

- (15) Jesse, S.; He, Q.; Lupini, A. R.; Leonard, D. N.; Oxley, M. P.; Ovchinnikov, O.; Unocic, R. R.; Tselev, A.; Fuentes-Cabrera, M.; Sumpter, B. G.; Pennycook, S. J.; Kalinin, S. V.; Borisevich, A. Y. Atomic-Level Sculpting of Crystalline Oxides: Toward Bulk Nanofabrication with Single Atomic Plane Precision. Small 2015, 11, 5895–5900.
- (16) Wan, Z.; Liu, R.; Savage, D. E.; Kuech, T. F.; Evans, P. G.; Schmidt, J. R. Kinetics and Mechanism of γAl_2O_3 Solid Phase Epitaxy on c-Plane Sapphire. *J. Phys. Chem. C* **2023**, *127*, 13207–13216.
- (17) Lindahl, E.; Abraham, M. J.; Hess, B.; van der Spoel, D. GROMACS 2019.6 Source code. 2020,
- (18) Stukowski, A. Visualization and analysis of atomistic simulation data with OVITO-the Open Visualization Tool. *Model. Simul. Mater. Sci. Eng.* **2009**, *18*, 015012.
- (19) Thomas, B. S.; Marks, N. Developing pair potentials for simulating radiation damage in complex oxides. *Nucl Instrum Methods Phys Res B* **2005**, *228*, 288–292.
- (20) Akhtar, M. J.; Akhtar, Z.-U.-N.; Jackson, R. A.; Catlow, C. R. A. Computer simulation studies of strontium titanate. *J. Am. Chem. Soc.* **1995**, *78*, 421–428.
- (21) McCoy, M. A.; Grimes, R. W.; Lee, W. E. Phase stability and interfacial structures in the SrO-SrTiO3 system. *Philosophical Magazine A* **1997**, *75*, 833–846.
- (22) Crawford, J.; Jacobs, P. Point defect energies for strontium titanate: A pair-potentials study. *Journal of Solid State Chemistry* **1999**, *144*, 423–429.
- (23) Zapol, P.; Pandey, R.; Gale, J. D. An interatomic potential study of the properties of gallium nitride. *J. Phys.: Condens. Matter* **1997**, *9*, 9517–9525.
- (24) Frenkel, D.; Smit, B. Understanding molecular simulation: from algorithms to applications; Academic Press San Diego, 2002; Vol. 2.

- (25) Mirskaya, K. Combining rules for interatomic potential functions of Buckingham form. *Tetrahedron* **1973**, *29*, 679–682.
- (26) Stöcker, H.; Hanzig, J.; Zschornak, M.; Mehner, E.; Jachalke, S.; Richter, C.; Hanzig, F.; Meutzner, F.; Leisegang, T.; Meyer, D. C. Strontium titanate: From symmetry changes to functionality. Cryst. Res. Technol. 2017, 52, 1600222.
- (27) Meyer, G. M.; Nelmes, R. J.; Hutton, J. Ferroelectrics 1978, 21, 461–462.
- (28) Liu, R.; Elleuch, O.; Wan, Z.; Zuo, P.; Janicki, T. D.; Alfieri, A. D.; Babcock, S. E.; Savage, D. E.; Schmidt, J. R.; Evans, P. G.; Kuech, T. F. Phase Selection and Structure of Low-Defect-Density γ Al₂O₃ Created by Epitaxial Crystallization of Amorphous Al₂O₃. ACS Appl. Mater. Interfaces 2020, 12, 57598–57608.
- (29) Steinhardt, P. J.; Nelson, D. R.; Ronchetti, M. Bond-orientational order in liquids and glasses. *Phys. Rev. B* **1983**, *28*, 784–805.
- (30) Rankin, J.; McCallum, J. C.; Boatner, L. A. The effect of annealing environments on the epitaxial recrystallization of ion-beam-amorphized SrTiO₃. J. Mater. Res. **1992**, 7, 717–724.
- (31) Simpson, T. W.; Mitchell, I. V.; McCallum, J. C.; Boatner, L. A. Hydrogen catalyzed crystallization of strontium titanate. *J. Appl. Phys.* **1994**, *76*, 2711–2718.
- (32) Wang, T.-C.; Juang, J.-Y.; Wu, K.-H.; Uen, T.-M.; Gou, Y.-S. Thermally activated diffusion observed by in situ reflection high energy electron diffraction intensity monitoring on interrupted SrTiO3 homoepitaxial growth. *Jpn. J. Appl. Phys.* **2004**, *43*, 771.
- (33) Sano, T.; Saylor, D. M.; Rohrer, G. S. Surface Energy Anisotropy of SrTiO₃ at 1400°C in Air. J. Am. Chem. Soc. 2003, 39, 1933–1939.

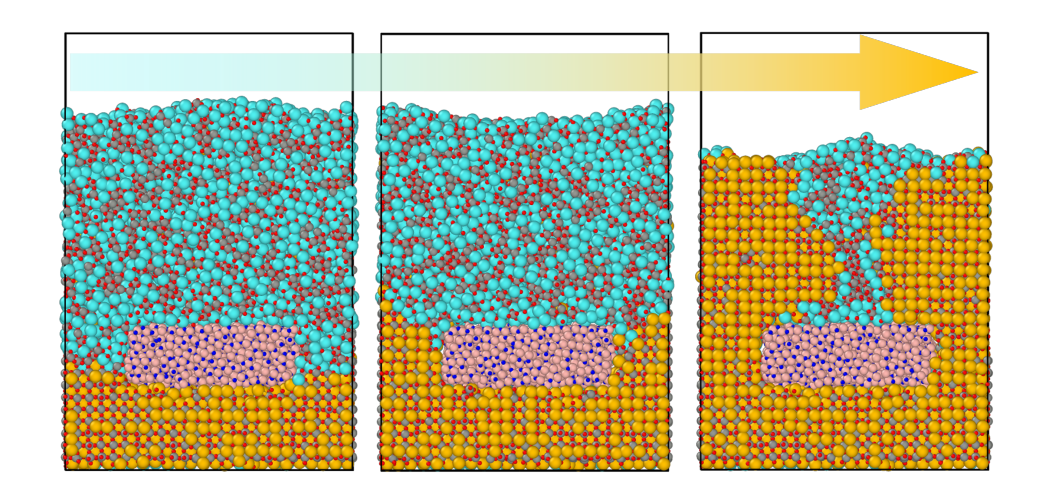
- (34) Rheinheimer, W.; Bäurer, M.; Chien, H.; Rohrer, G. S.; Handwerker, C. A.; Blendell, J. E.; Hoffmann, M. J. The equilibrium crystal shape of strontium titanate and its relationship to the grain boundary plane distribution. *Acta Mater*, **2015**, *82*, 32–40.
- (35) Ringe, E.; Van Duyne, R. P.; Marks, L. D. Kinetic and thermodynamic modified Wulff constructions for twinned nanoparticles. *J. Phys. Chem. C* **2013**, *117*, 15859–15870.
- (36) Boukouvala, C.; Daniel, J.; Ringe, E. Approaches to modelling the shape of nanocrystals. *Nano Convergence* **2021**, *8*, 1–15.
- (37) Tersoff, J. Enhanced solubility of impurities and enhanced diffusion near crystal surfaces. *Physical review letters* **1995**, *74*, 5080.
- (38) Ediger, M. D.; de Pablo, J.; Yu, L. Anisotropic vapor-deposited glasses: hybrid organic solids. *Accounts of chemical research* **2019**, *52*, 407–414.
- (39) Sun, Y.; Zhu, L.; Kearns, K. L.; Ediger, M. D.; Yu, L. Glasses crystallize rapidly at free surfaces by growing crystals upward. *Proceedings of the National Academy of Sciences* **2011**, *108*, 5990–5995.
- (40) Hirth, J. P. Theory of Dislocations, 2nd ed.; Wiley, 1983; pp 637–681.
- (41) Young, T. III. An essay on the cohesion of fluids. *Philosophical Transactions of the Royal Society of London* **1805**, *95*, 65–87.
- (42) Zurbuchen, M.; Tian, W.; Pan, X.; Fong, D.; Streiffer, S.; Hawley, M.; Lettieri, J.; Jia, Y.; Asayama, G.; Fulk, S.; others Morphology, structure, and nucleation of out-ofphase boundaries (OPBs) in epitaxial films of layered oxides. J. Mater. Res. 2007, 22, 1439–1471.

For Table of Contents Use Only

Mechanisms of three-dimensional solid-phase epitaxial crystallization of strontium titanate

Tesia D. Janicki^{1,2}, Rui Liu³, Soohyun Im³, Zhongyi Wan¹, Serkan Butun⁴, Shaoning Lu⁴, Nasir Basit⁴, Paul M. Voyles³, Paul G. Evans³, and J. R. Schmidt¹

- ¹ Department of Chemistry, University of Wisconsin-Madison, Madison, WI 53706
- 2 Department of Computational Materials, Sandia National Laboratories, Albuquerque, NM $87185\,$
- ³ Department of Materials Science and Engineering, University of Wisconsin-Madison, Madison, WI 53706
- 4 Northwestern University Micro/Nano Fabrication Facility, Northwestern University, Evanston IL, 60208



TOC: Simulation snapshots portray progression of strontium titanate crystallization over an inert amorphous mask.